Applied Thermal Engineering 241 (2024) 122325

Contents lists available at ScienceDirect

Applied Thermal Engineering

journal homepage: www.elsevier.com/locate/apthermeng

Research Paper

Enhanced boiling heat transfer via microporous copper surface integration in a manifold microgap

Kiwan Kim [a], Daeyoung Kong [b,c], Yunseo Kim [a], Bongho Jang [d], Jungwan Cho [e], Hyuk-Jun Kwon [d], Hyoungsoon Lee [a,c,*]

[a] Department of Intelligent Energy and Industry, Chung-Ang University, Seoul 06974, South Korea
[b] Mechanical Engineering Department, Stanford University, Stanford, CA 94305, United States
[c] School of Mechanical Engineering, Chung-Ang University, Seoul 06974, South Korea
[d] Department of Electrical Engineering and Computer Science, Daegu Gyeongbuk Institute of Science & Technology, Daegu 42988, South Korea
[e] School of Mechanical Engineering, Sungkyunkwan University, Suwon-si, Gyeonggi-do 16419, South Korea

A R T I C L E I N F O

Keywords:
Embedded cooling
Manifold microgap
Microporous surface
Copper inverse opal
Flow boiling
Thermal management

A B S T R A C T

Heat flux dissipation from electronic devices has increased with their miniaturization owing to the increasing performance demands and development of microfabrication technologies. Improving the heat transfer performance is crucial for enhancing heat dissipation. However, this often leads to an increase in pressure drop, which reduces energy efficiency. Microgap heat sink is a promising approach in this regard owing to its geometrical simplicity and facile fabrication while providing heat transfer performance comparable to that of microchannel heat sinks with substantially lower pressure drops. In this study, we develop a manifold microgap heat sink integrated with a porous copper surface that effectively enhances heat transfer while using significantly low pumping power. A three-dimensional liquid routing manifold is used to achieve better flow distribution and alleviate temperature non-uniformity while providing improved heat transfer by enabling jet impingement and mixing of the thermal boundary layer on the microgap surface with minimal additional pressure drop. Moreover, a microscale inverse opal structure is used to facilitate nucleate boiling on the microgap surface, which improves heat transfer while maintaining a relatively low flow resistance. A maximum heat flux of 322.8 W/cm^2 was achieved at the mass flux of 472 kg/m^2 s, and the corresponding pressure drop and maximum heater temperature were 0.6 kPa and 140 °C, respectively. The coefficient of performance (COP) achieved herein was significantly higher than those reported in previous relevant studies, indicating that the proposed cooling technique can potentially be used for energy-efficient thermal management in electronics devices.

1. Introduction

Wide bandgap semiconductors such as gallium nitride on silicon (GaN-on-Si) have attracted considerable attention because of their favorable properties and advantages over traditional semiconductors, such as higher breakdown voltage, higher operating temperature, higher electron mobility, and higher radiation tolerance [1,2], making them a promising candidate for advanced electronic applications. However, these advantages lead to extremely high heat fluxes near the junction, resulting in increased temperature non-uniformity and, consequently, compromised electrical performance [3]. Local hotspots cause the incipience of dryout and flow instability, which affect the durability and robustness of electronic devices [4,5]. Furthermore, the dissipation of excessive heat flux necessitates a larger quantity of coolant to maintain optimal operating conditions. This increased coolant requirement leads to a substantial rise in pressure drop within the cooling system, resulting in a significant escalation of energy consumption and associated electricity expenses [6]. Moreover, it can cause critical issues in the long-term operation of electronic devices, including increased vibration and potential malfunctions [7]. To address sustainable and cost-effective thermal management in high-heat-flux electronics, it is crucial to achieve enhanced thermal performance with minimal pumping power [8].

Researchers have investigated various active cooling schemes for high-heat-flux electronics such as microchannels [9–11], jet impingements [12–14], and pin fins [15–17]. A two-phase heat sink that uses a mini/microgap is a promising thermal management strategy because it is relatively simple to fabricate [18] while providing adequate cooling

* Corresponding author at: School of Mechanical Engineering, Chung-Ang University, Seoul 06974, South Korea.
E-mail address: leeh@cau.ac.kr (H. Lee).

https://doi.org/10.1016/j.applthermaleng.2023.122325
Received 26 May 2023; Received in revised form 28 November 2023; Accepted 29 December 2023
Available online 12 January 2024

Nomenclature

A	area
COP	coefficient of performance
G	mass flux
h	heat transfer coefficient
H	height
k	thermal conductivity
L	length
ΔP	pressure drop
P	pressure
P_{pump}	pumping power
q''	heat flux
Q	heat
R	thermal resistance
Re	Reynolds number
t	thickness
T	temperature
W	width

Greek symbols

ε	emissivity
ρ	density

Subscripts

adv	advection
avg	average
cond	conduction
conv	convection
eff	effective
f	fluid
h	heater
in	inlet
max	maximum
out	outlet
s	silicon
tot	total
w	wall

performance with a relatively small pressure drop [19,20]. Yang and Fujita [21] investigated the heat transfer performance and flow patterns of a minigap with gap heights of 0.2, 0.5, 1, and 2 mm. They observed relatively high heat transfer coefficients for the channels with lower gap heights (0.2 mm and 0.5 mm) in the lower-quality regions while similar heat transfer coefficient trends as those observed for minigaps of conventional heights were observed for the channels with higher gap heights (1 mm and 2 mm). Kim *et al.* [22] investigated the two-phase heat transfer characteristics of FC-72 in a microgap heat sink. They reported that a higher microgap height of 500 μm yielded a higher area-averaged heat transfer coefficient of 15.5 kW/m^2 K compared to that yielded by a lower microgap height of 110 μm. Sheehan and Bar-Cohen [23] examined a 210-μm-high microgap heat sink with FC-72 as the working fluid. They analyzed wall temperature fluctuations under varying vapor qualities and heat fluxes, revealing independent variations linked to flow thermodynamic quality and wall heat flux. The author attributed these fluctuations to a complex interplay of channel and local instabilities, periodically involving dryout and re-wetting. Alam *et al.* [24] identified the effects of variations in microgap height and claimed that heat sinks with smaller microgap heights provide superior heat transfer characteristics. Moreover, they demonstrated that smaller microgap heights increase the pressure drop as the heat flux increases while larger microgap heights ensure that the pressure drop remains relatively uniform. In another study [19], the heat transfer performances of microgap and microchannel heat sinks were studied by comparing a 12.7 × 12.7 mm^2 heat sink with a 190 μm height gap to a microchannel heat sink with a height of 385.7 μm and width of 208.28 μm. In terms of thermal management performance, the microchannel heat sink outperformed the microgap heat sink at low heat fluxes owing to earlier formations of slug and annular flows. However, at high heat fluxes, the heat transfer performance of the microgap heat sink improved owing to the delayed dryout phase. Furthermore, the microgap heat sink provided better temperature uniformity and had a smaller temperature gradient on its heater surface under all the experimental conditions.

Several investigations have been conducted to enhance thermo-hydraulic performance by using heat sinks with modifications such as increased effective heat transfer area [25–27]; structures for stabilizing fluid flow [18,28,29]; or surface treatments such as roughened surface [30], nanowires [31], and woven mesh coating [32]. Han *et al.* [25] examined subcooled flow boiling in a microgap heat sink with staggered circular micro pin-fins. They observed a declining trend in the two-phase heat transfer coefficient with increasing heat flux, particularly less prominent at higher levels. Notably, instead of conventional bubbly or slug flow patterns, they noted the formation of triangular-shaped vapor wakes at bubble nucleation sites. Mathew *et al.* [26] developed a hybrid heat sink design that combined microchannels in the upstream with a microgap in the downstream. In terms of thermal performance, the hybrid design outperformed the microgap, but its pressure drop was higher. Moreover, although the thermal performance of the aforementioned hybrid design was inferior to that of a microchannel, its pressure drop was lower, and it provided more stable boiling conditions. Yin *et al.* [27] proposed a modified microgap design that featured shortened micro pin fins in the downstream area. This modified design augmented boiling heat transfer, exhibiting a higher heat transfer coefficient than that of a smooth-surfaced region. However, the authors noted that their design induced a higher pressure drop than the smooth microgap because of the increased frictional pressure drop in the micro pin fins area. Tamanna and Lee [18,28] studied the thermo-hydraulic characteristics of an expanded silicon microgap heat sink. Their findings indicated that the expanded microgap retained a more uniform wall temperature, reduced flow instability, and delayed dryout, compared to a straight microgap heat sink. Klugmann *et al.* [29] assessed the heat transfer performance of a minigap and mini-channel. They demonstrated that the mini-channel had a higher heat transfer coefficient than that of the minigap with the same cross-sectional area. They proposed modified microgap heat sinks with dimples and cross-nuts on the surface and demonstrated that the microgap with cross-nuts had reduced flow resistance because it reduced fluid maldistribution. Alam *et al.* [30] identified the effects of surface roughness on the thermal and hydraulic performance of a microgap heat sink. Three different surface roughness, R_a = 0.6 μm, 1.0 μm and 1.6 μm were used to examine the effect of surface finish. They claimed that surface roughness increased the nucleate site density and boiling heat transfer. Although an increase in roughness affected the instability of inlet pressure, it had no significant adverse effect on the tested microgap heat sinks. Morshed *et al.* [31] studied the thermal performance of a copper nanowire surface microgap with a height of 360 μm and compared the results to those of bare surfaces. The copper nanowire surfaces reduced the superheat needed for the onset of boiling (ONB) and enhanced the single- and two-phase heat transfer performance by approximately ~25% and ~56%, respectively. The pressure drop in the single-phase regime increased by up to 20%, but it did not change significantly in the fully developed two-phase regime. Dai *et al.* [32] developed a flow separation structure in a woven copper-mesh-coated microgap. This flow separation structure inhibited boundary layer growth in the single-phase flow, thereby

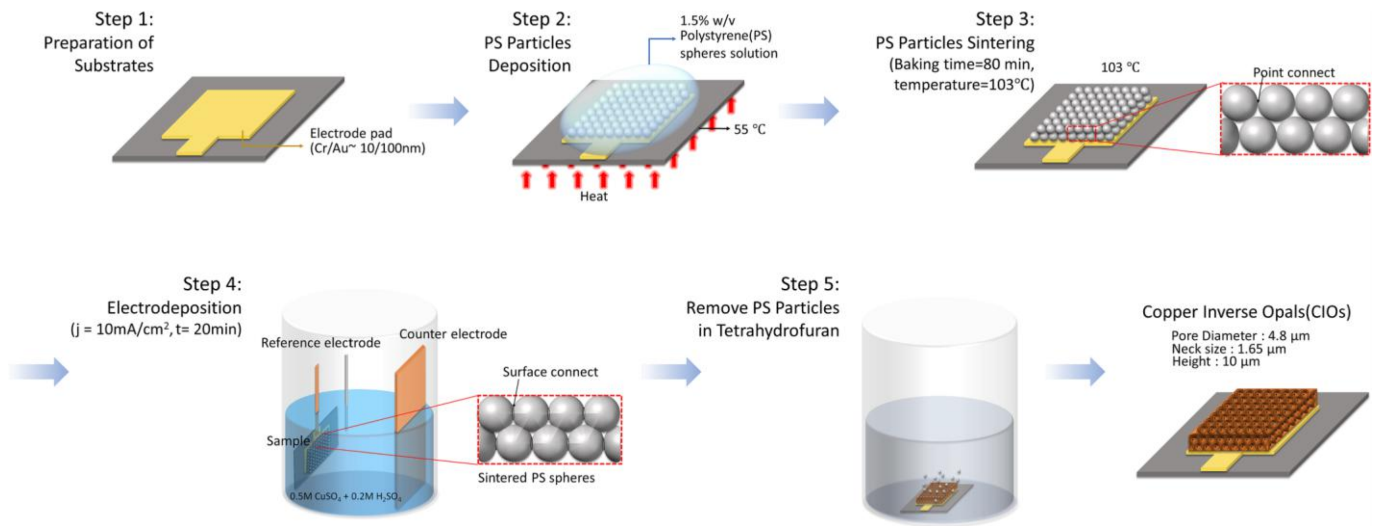

Fig. 1. Schematic illustration of copper inverse opal synthesis. *Step 1*: The 5 mm × 5 mm chromium/gold electrode on the silicon wafer was prepared as the substrate. *Step 2:* 70 μL of 1.5% weight/volume PS/water suspension was dispensed on the gold electrode of the silicon wafer by using the drop casting method. Polystyrene (PS) spheres measuring 4.8 μm in diameter were deposited on the silicon wafer to create a sacrificial template, and the substrate was heated to 55 ℃ on a hot plate. *Step 3:* After all the water evaporated, the PS spheres were sintered in an oven at 103 ℃ for 80 min to form ~1.65-μm necks. *Step 4*: Potentiostatic electrodeposition was performed at a constant current density of 10 mA/cm^2 for 20 min to achieve 2–2.5 layers of copper inverse opal (CIO) surface. *Step 5*: After deposition of the copper layer, the silicon wafer was immersed in tetrahydrofuran (THF) for 24 h to dissolve the PS sphere template from the CIO surface.

reducing the temperature change in the direction of flow, and suppressed the expansion of bubbles in the two-phase flow. During convective boiling, the average wall temperature decreased by 2.9 ± 0.6 ℃ when the mass flux was 83 kg/m^2 s, and the pressure drop decreased by 60.4%. The pressure drop decreased when the flow area in the auxiliary channel was increased and the rate of bubble expansion was regulated. In the aforementioned studies, diverse techniques were used to enhance the heat transfer performance of microgaps, but most of these methods resulted in a substantial pressure drop increase as the heat transfer efficiency improved, which seems to be an inevitable outcome [32].

Herein, we develop a manifold microgap heat sink that features a microporous copper coating, which effectively enhances the heat transfer performance with relatively minimal additional pressure drop. A three-dimensional (3D) liquid routing manifold to the microgap heat sink results in a well-distributed flow supply that alleviates temperature non-uniformity over the heated area. Moreover, this configuration improves heat transfer through superior mixing of the thermal boundary layer and jet impingement. Furthermore, copper inverse opal (CIO) coating on the microgap provides a large effective heat transfer area

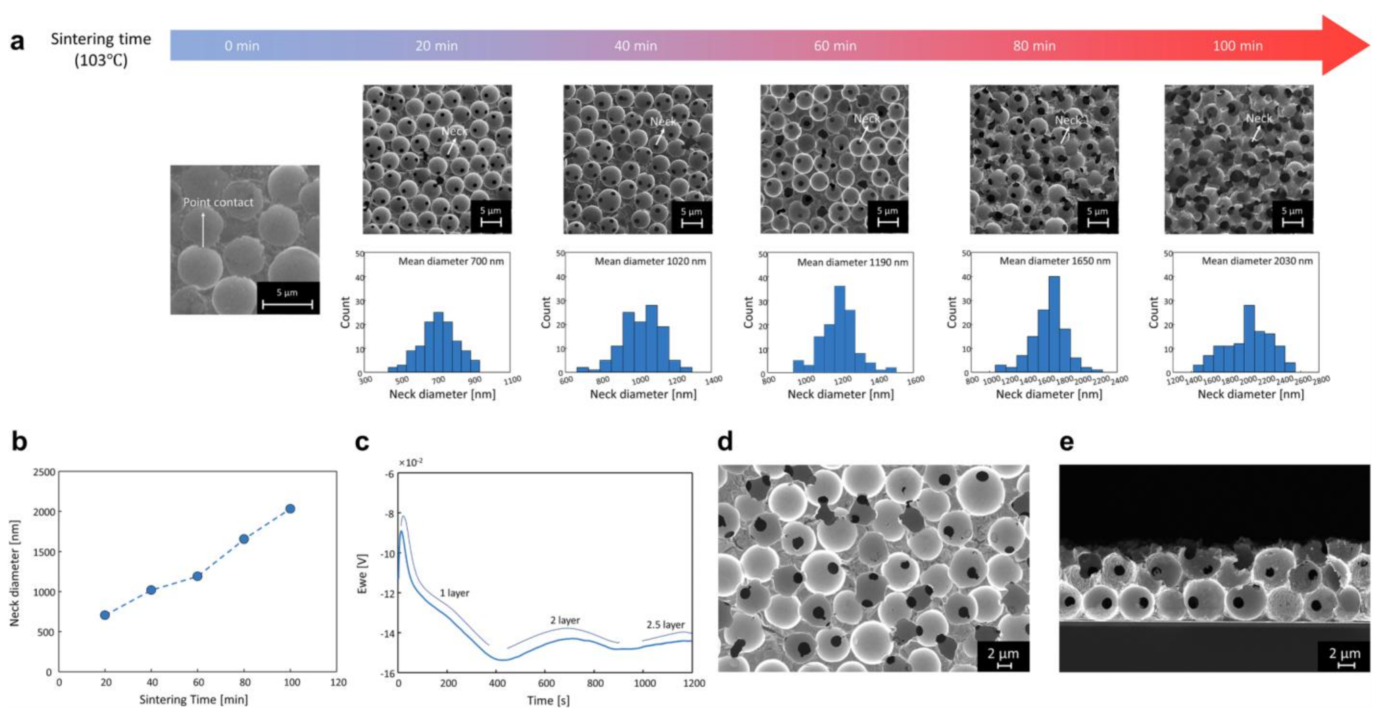

Fig. 2. Representative images of 2–2.5 CIO layers with different neck sizes. (a) CIOs subjected to different sintering times of 20–100 min. (b) Mean diameter of CIO depending on sintering time. (c) Galvanostatic electrodeposition characteristic of 2–2.5 layers of electrodeposited CIO. Field emission scanning electron microscopy (FE-SEM) images of CIO showing. (d) Top view. (e) Cross-sectional view.

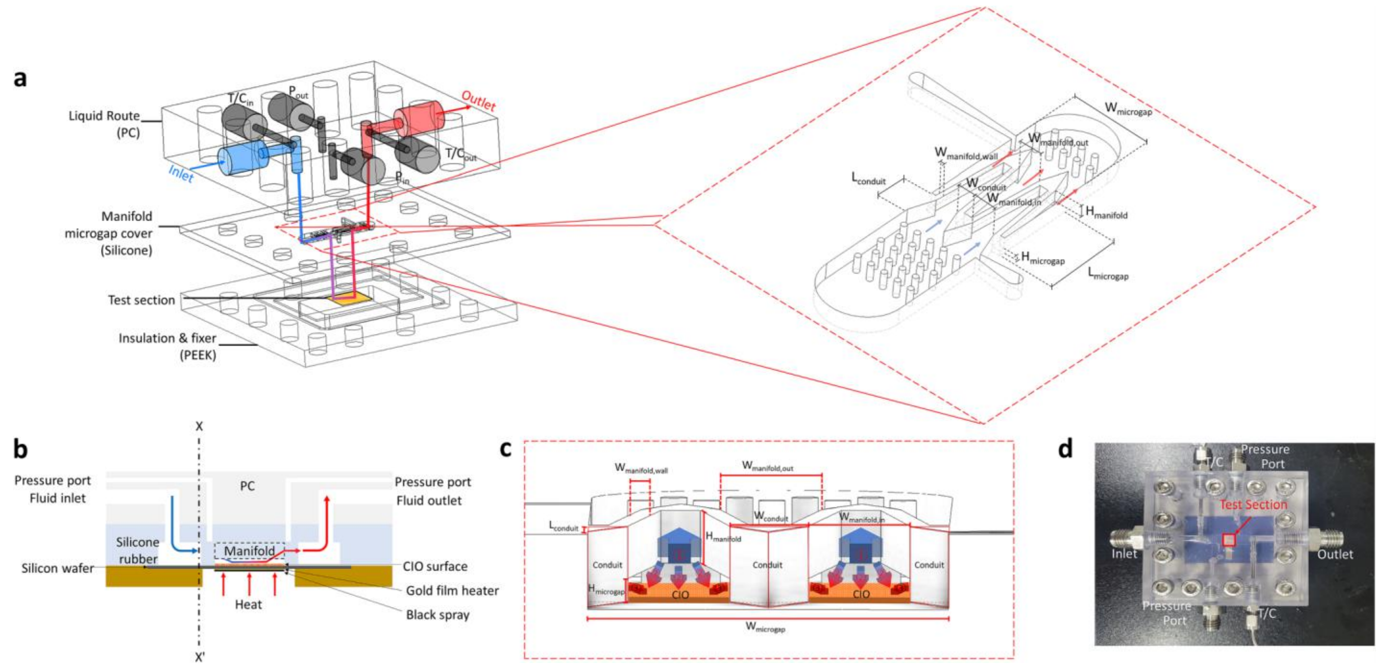

Fig. 3. Schematic configurations of test module. (a) Schematic of manifold microgap test module assembly and detailed manifold microgap geometry representing the length *L*, width *W*, and height *H*. (b) Cross-sectional image of assembled test module showing the coolant path through the test section. (c) Cross-sectional image of manifold microgap with CIO including the coolant path in the test section (axis X-X′ in Fig. 3(b)). (d) Photograph of manifold microgap heat sink made of silicone.

with a relatively low flow resistance [33]. We perform a thermo-hydraulic analysis to demonstrate that the proposed manifold micro-gap heat sink with a porous surface can provide outstanding thermal management capabilities with superior temperature distribution and low pressure drop.

2. Methods

2.1. Porous copper inverse opal synthesis

We utilized a manifold microgap heat sink coated with CIO. CIO offers several benefits over other porous copper surfaces in terms of thermal management of high-heat-flux electronic devices. The CIO fabrication process does not require high-temperature metal sintering, which may damage electronic devices. Therefore, CIO can be easily deposited directly on the substrates of electronic devices.

We fabricated a porous inverse opal structure on a microgap surface by electrodepositing copper, as illustrated in Fig. 1. First, 70 μL of 1.5% weight/volume polystyrene (PS)/water suspension was dispensed on the 5 mm × 5 mm gold electrode of a silicon wafer by using the drop casting method. PS particles measuring 4.8 μm in diameter were used in the sacrificial template. Then, the silicon wafer was heated to 55 ℃ on a hot plate. After all the water evaporated, the PS spheres were sintered in an oven at 103 ℃ for 80 min to create ~1.65 μm necks between the contact surfaces of the PS spheres. After the wafer was cooled to ambient temperature, 5 μL of ethanol was dropped on the PS template before it was immersed in an aqueous 0.5 M $CuSO_4$ + 0.2 M H_2SO_4 electrolyte solution. Potentiostatic electrodeposition (BioLogic SP-300) was performed under a constant current density of 10 mA/cm^2 for 20 min to form 2–2.5 layers of the CIO surface (~10 μm height). After the CIO layer was deposited, the silicon wafer was immersed in tetrahydrofuran (THF) for 24 h to dissolve the PS sphere template from the CIO. Fig. 2 shows representative images of CIO structures with different sintering times ranging from 20 to 100 min. The neck sizes varied depending on the sintering time, ranging from 700 nm post 20 min sintering to 2000 nm post 100 min sintering. The oscillations indicated that the electrochemically accessible surface area changed as copper was filled in around the curved surfaces of the densely packed spheres on each opal layer [34]. Therefore, 2–2.5 layers of inverse opal structures were deposited during the electrodeposition process.

2.2. Design and fabrication of manifold microgap cooling

Fig. 3 shows the detailed schematic configurations and a photograph of the test module assembly. Polycarbonate (PC) was fabricated to create fluid route and holes for measuring temperature and pressure. A manifold microgap structure was fabricated using silicone (SORTA-Clear 40). A mold of the manifold microgap structure was fabricated by processing an acrylic plate by using a CNC machine (Boardtech & David, TOOLI-34P). Silicone was poured on the acrylic mold, and internal air was degassed. After the internal air was completely degassed, the silicone was cured at room temperature for more than 24 h.

Fluid flows in through the inlet plenum and is introduced to the microgap through two manifold inlets. The inlet and outlet plenums feature relatively large pin fins, approximately 300 μm in diameter, which provide an evenly distributed flow into the manifold inlets while providing structural support. A reducing conduit, measuring 1800 μm in length, is placed near the inlet and outlet of the manifold. Its purpose is to minimize pressure losses caused by abrupt changes in area and to obstruct direct fluid flow from the microgap to the outlet. The fluid

Table 1
Dimensions of manifold microgap structure.

Geometry	$W_{manifold\ wall}$	$W_{manifold\ inlet}$	$W_{manifold\ outlet}$	$H_{manifold}$	$W_{conduit}$	$L_{rconduit}$	$W_{microgap}$	$H_{microgap}$	$L_{migrogap}$
Dimension (μm)	300	1550–600	600–1550	800	1800	1800	5500	1150	5000

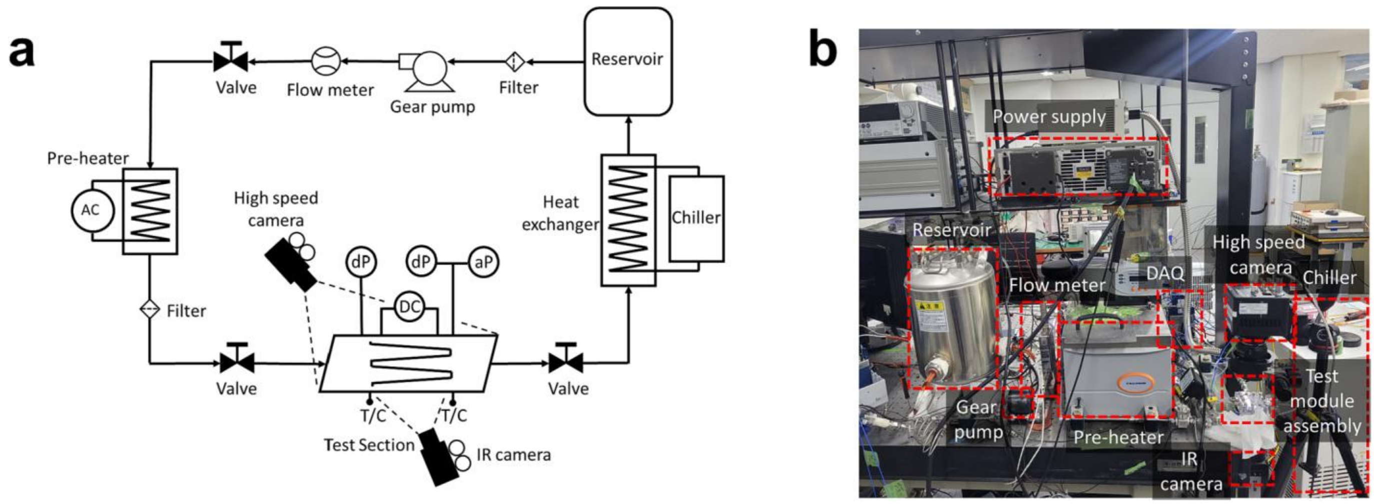

Fig. 4. Experimental setup for thermo-hydraulic performance evaluation. (a) Schematic overview of flow loop. (b) Photograph of experimental apparatus.

introduced into the microgap cools a 5 × 5 mm^2 heater and exits from the outlet plenum through three manifold outlets. Each manifold wall has a uniform wall thickness of 300 μm and height of 800 μm. The manifold walls are tapered, and their width decreases linearly from 1550 μm to 600 μm to improve flow distribution in the microgap. The microgap is maintained at a height of 350 μm. Table 1 summarizes the detailed geometrical parameters of the manifold microgap used in this study.

The silicon wafer test section was located on a polyether ether ketone (PEEK). The silicone manifold microgap and PC were placed in that order on the PEEK and bolted for fittings and wiring connections; moreover, they provided soft compressive strength to prevent fluid leakage without changing the microgap height.

2.3. Flow loop for thermo-hydraulic evaluation

The thermo-hydraulic characteristics of the manifold microgap were evaluated using the flow loop setup shown in Fig. 4(a). We employed deionized water as the working fluid in the experiment and removed any dissolved gases by boiling it vigorously for approximately 30 min in a reservoir before the test. The working fluid was circulated through the flow loop by using a magnetically driven gear pump (Micropump GA-T23). A Coriolis mass flow meter (Bronkhorst KIF510) was used to measure the flow rate of the working fluid. A preheater (TECHNE TE-10D) was installed to set the fluid inlet temperature to a fixed value. We monitored the heater temperature in our setup using a thermal-infrared camera (FLIR A655sc) and captured images of boiling bubbles with a high-speed camera (Photron FASTCAM Mini UX100). The gold thin-film serpentine shaped heater was coated with black spray paint, and we calibrated its surface emissivity ($\varepsilon = 0.93$) in a prior experiment. Its surface emissivity ($\varepsilon = 0.93$) was calibrated in our previous experiment [35]. A plate heat exchanger was used in combination with a liquid circulation chiller (Jeiotech HH-20) to cool the DI water passing through the test section. The fluid temperature values at the inlet and outlet were measured using K-type thermocouples. An absolute pressure transducer (TRAFAG ECT1.0A) was installed at the test section outlet to measure the outlet pressure, and differential pressure transducers (OMEGA PX409) were installed at the inlet and outlet of the test section to measure the pressure drop. Fig. 4(b) presents a photograph of the experimental apparatus.

2.4. Test procedure, operating conditions, and uncertainty

Some of the heat supplied was dissipated through the test section assembly and heater surface through conduction, natural convection, and radiation heat transfer. To calculate this heat loss, the test section was heated in increments without any fluid flowing, and average heater temperature was measured in the steady state. This procedure was repeated until the maximum heater temperature exceeded 140℃. The experimentally calibrated Q_{loss} with respect to the heater temperature can be expressed as follows:

$$Q_{loss} = 0.04 \times T_{h,avg} - 0.56 \tag{1}$$

The thermo-hydraulic evaluation was started by setting the coolant mass flux by adjusting the speed (rpm) of the micropump. Simultaneously, the outlet pressure was set to the desired value by using the control valve. Then, the coolant was preheated using a preheater to a temperature of around 20 ℃ before it was supplied to the test section. A power supply unit (HP 6030A) was used to provide heat to the gold thin-film heater. The voltage divider circuit, which included two resistors with resistances of 39 kΩ ± 5% and 1 kΩ ± 1%, as well as a 0.1 Ω ± 1% shunt resistor, was used to measure the total heat input. Once the steady state was reached, the coolant pressure and temperature were measured using an NI Compact DAQ system connected to LabVIEW software. Meanwhile, the heater temperature and boiling bubble images were recorded using the infrared camera and high-speed camera, respectively. After data acquisition, the heat flux was increased in increments of 2.5 W (10 W/cm^2) until the maximum heater temperature reached around 140 ℃ to prevent damage to the heater. After the test for one mass flow rate was completed, the flow rate was adjusted, and the above sequence was repeated. The operating conditions used in this study were as follows: heat flux $q'' = 10.3$–322.8 W/cm^2, mass flux $G = 156$–472 kg/m^2 s, Reynolds number $Re = 183.9$–582.6, and pressure drop $dP = 0.18$–0.6 kPa. Here, the mass fluxes were determined based on the cross-sectional area of the microgap. The inlet temperature and outlet pressure were maintained at $T_{in} = 20.1$–21.9 ℃ and $P_{out} = 106.7$–108.5 kPa, respectively.

The accuracy of the K-type thermocouples used herein was ±0.4%. The accuracy of the calibrated IR measurement was ±2% of the reading. The Coriolis mass flow meter used herein had an accuracy of ±0.1%. The accuracies of the differential pressure transducer and absolute pressure transducer were ±0.08% and ±0.5%, respectively. The data points for which the uncertainty of the heat transfer coefficient exceeded 10% were excluded. Consequently, the mean uncertainties in the pressure drop and heat transfer coefficient, as calculated using the method proposed by Taylor and Kuyatt [36], were ±8.9% and ±6.2%, respectively.

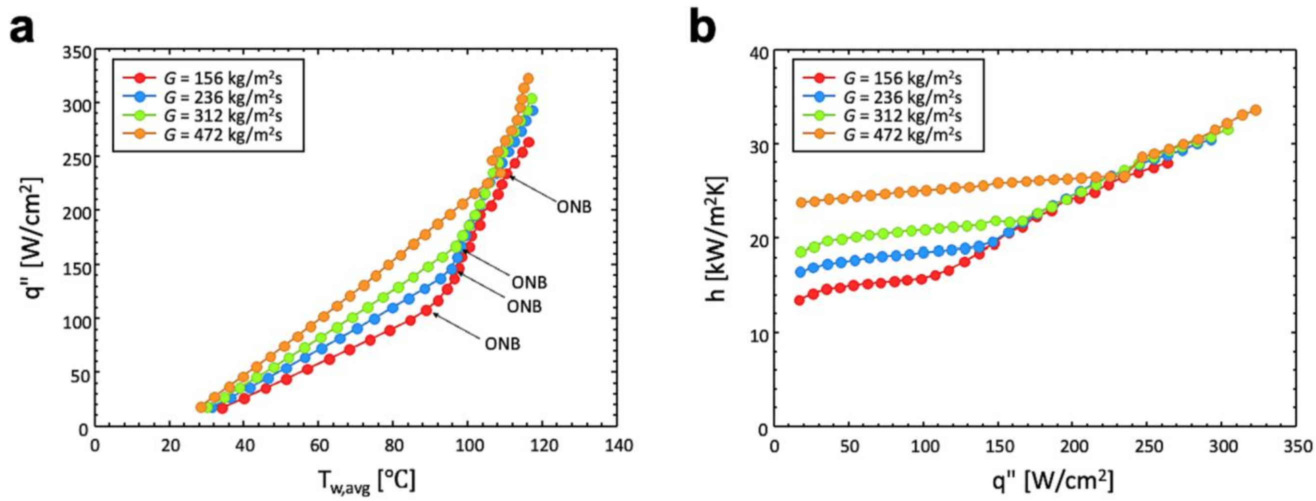

Fig. 5. Heat transfer performance of manifold microgap heat sink. (a) Boiling curves: heat flux versus wall temperature for four different mass fluxes. (b) Heat transfer coefficient curves as a function of heat flux.

2.5. Data reduction

The effective heat Q_{eff} was determined by subtracting the heat lost from the heater to the surroundings from the power supplied.

$$Q_{eff} = Q - Q_{loss} \tag{2}$$

where Q is the power to the test section from the power supply, and it is determined as the product of the voltage and current supplied to the film heater. The effective heat flux q''_{eff} is determined as the ratio of effective heat to the surface area of the test section, $A = L \times W$, where L and W denote the length and width of the test section, respectively.

$$q''_{eff} = \frac{Q_{eff}}{A} \tag{3}$$

The heat transfer coefficient is determined as follows:

$$h = \frac{q''_{eff}}{T_{w,avg} - T_{f,in}} \tag{4}$$

where $T_{f,in}$ is the inlet temperature of coolant, and $T_{w,avg}$ is the average wall temperature determined from the averaged heater temperature $T_{h,avg}$ by subtracting conduction loss through the silicon substrate.

$$T_{w,avg} = T_{h,avg} - \frac{q''_{eff} t_s}{k_s} \tag{5}$$

where t_s denotes thickness, and k_s denotes the thermal conductivity of the silicon substrate.

The thermal and hydraulic performances were characterized by calculating the total thermal resistance, pressure drop, and the corresponding coefficient of performance (COP). The total thermal resistance can be calculated as follows:

$$R_{tot} = R_{adv} + R_{cond} + R_{conv} = \frac{T_{h,avg} - T_{f,in}}{Q_{eff}} \tag{6}$$

where R_{adv}, R_{cond}, and R_{conv} denote the advection thermal resistance, conduction thermal resistance and convection thermal resistance, respectively.

$$R_{adv} = \frac{T_{f,out} - T_{f,in}}{Q_{eff}} \tag{7a}$$

$$R_{cond} = \frac{T_{h,avg} - T_{w,avg}}{Q_{eff}} \tag{7b}$$

$$R_{conv} = \frac{T_{w,avg} - T_{f,out}}{Q_{eff}} \tag{7c}$$

Pumping power is calculated as follows:

$$P_{pump} = \frac{GA\Delta P}{\rho} \tag{8}$$

Here, G is the mass flux, and A is the cross-sectional area of the microgap. ΔP is the pressure drop, and ρ is the averaged coolant density.

COP represents the ratio of heat flux to the pumping power essential to sustain a specific level of heater temperature rise. Consequently, a higher COP implies a reduced cost in maintaining the desired thermal performance. In this study, we establish a temperature rise of 25 ± 5 ℃ (up to the maximum heater temperature) for the purpose of comparing COP.

$$COP = \frac{q''_{25^\circ C}}{P_{pump}} \tag{9}$$

where $q''_{25^\circ C}$ denotes the required heat flux to raise the heater temperature by 25 ± 5 ℃, ultimately reaching the maximum heater temperature.

3. Results and discussion

3.1. Thermo-hydraulic performance characteristics

We first evaluated the heat transfer performance of the manifold microgap heat sink coated with CIO for four different mass fluxes G = 156, 236, 312, and 472 kg/m^2 s, as shown in Fig. 5. Here, q'' denotes the wall heat flux measured using the voltage divider, and $T_{w,avg}$ is the averaged wall temperature. Owing to the increase in convective heat transfer, the slope increased slightly as the mass flux increased before reaching the ONB. As the mass flux increased, the ONB occurred at higher wall superheats, as reported in many microgap and microchannel studies [26,37,38]. After the incipience of boiling, the slopes of the curve were almost similar for different mass fluxes because nucleate boiling became a dominant heat transfer mechanism. The maximum heat fluxes of 263.6, 292.9, 304.1, and 322.8 W/cm^2 were dissipated by mass fluxes of 156, 236, 312, and 472 kg/m^2 s, respectively.

Fig. 5(b) shows the changes in the heat transfer coefficient in relation to the heat flux. As the mass flux increased, the heat transfer coefficient in the single-phase region increased marginally. As boiling occurred because of the increase in heat flux, the heat transfer coefficient increased significantly. At this stage, the effect of mass flux was

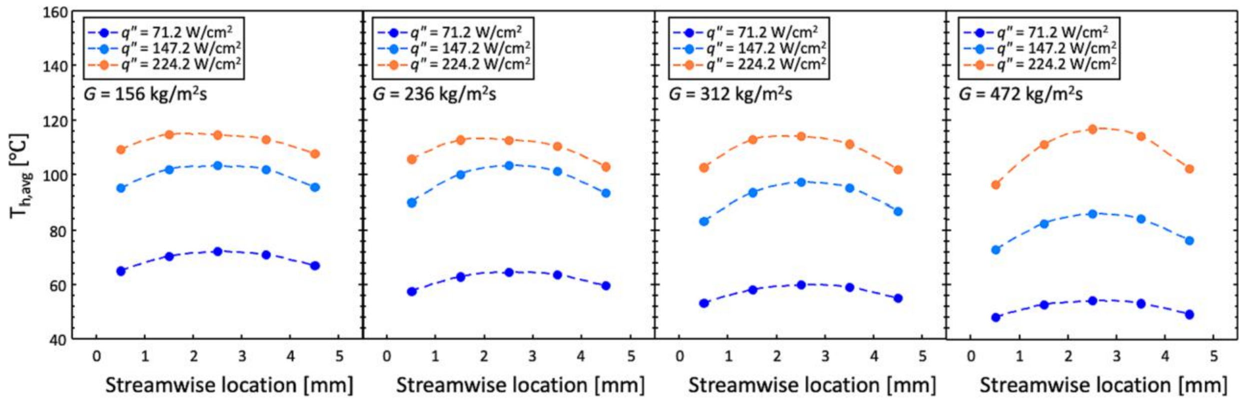

Fig. 6. Averaged heater temperature at five different streamwise locations. The heated area is divided into five regions along the flow direction, and the area-averaged temperatures of each region are compared under three representative heat fluxes.

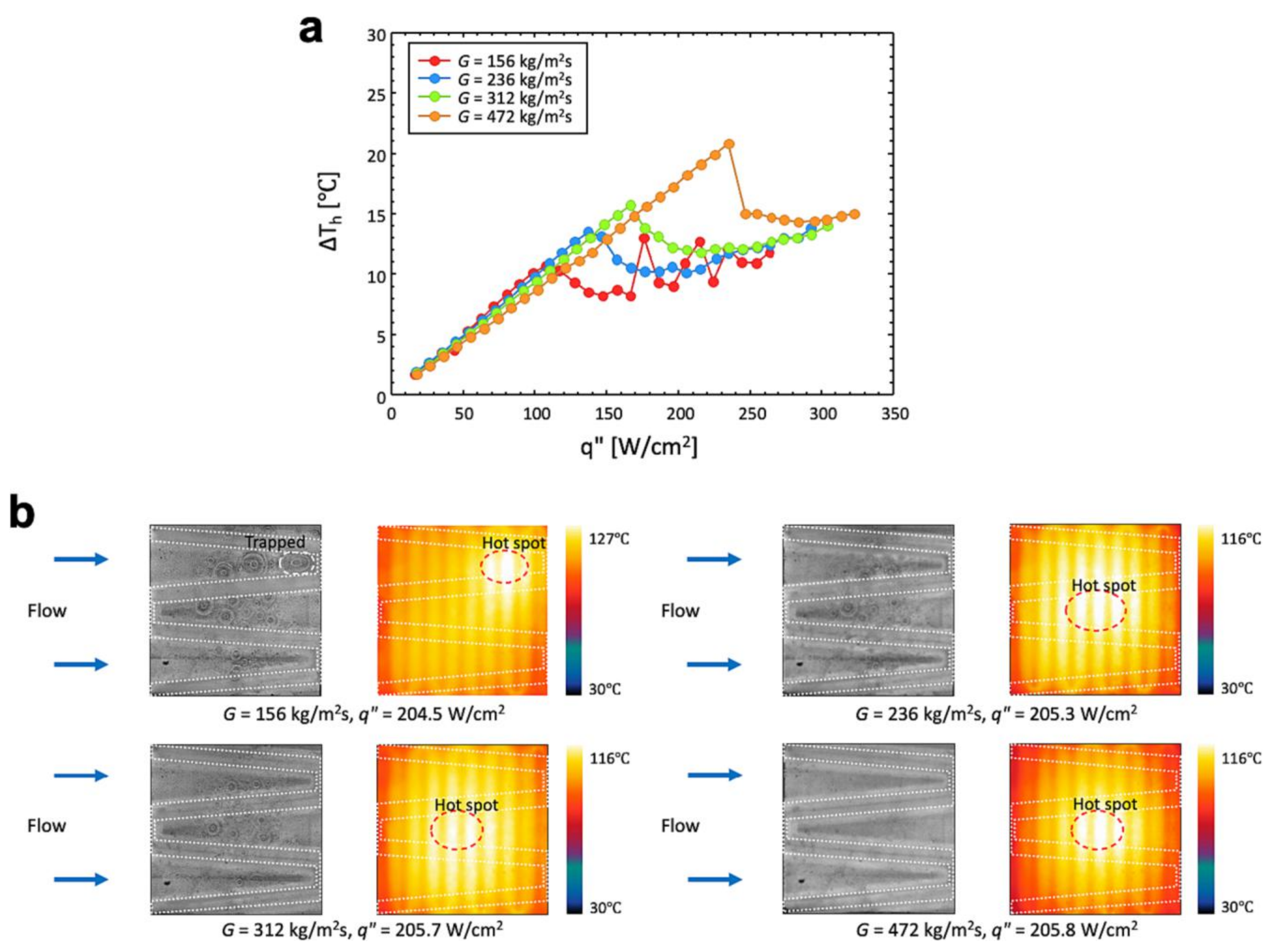

Fig. 7. Temperature non-uniformity of heated surface. (a) Difference between the maximum and average temperatures of the heater with respect to heat flux. (b) Flow visualization images and corresponding thermal images of heater surface at heat flux of $q'' \sim 205$ W/cm^2. The interior of the manifold wall is transparent, and the boundary is indicated by a dashed white line.

negligible because the nucleate boiling heat transfer was dominant. When the mass flux was 156 kg/m^2 s, the heat transfer coefficient was 16.1 kW/m^2 K just before ONB, and it increased to up to 27.9 kW/m^2 K when the heat flux was 263.6 W/cm^2. The highest mass flux of 472 kg/m^2 s led to a heat transfer coefficient of 26.5 kW/m^2 K just before the ONB, and it increased to up to 33.6 kW/m^2 K when the heat flux was set to 322.8 W/cm^2.

Fig. 6 shows the heater temperatures at five different streamwise locations for three representative heat fluxes of ~70, 150, and 225 W/cm^2 for each mass flux. The heater area is divided into five regions along the streamline, and the average heater temperature in each region was determined from IR thermal images. The maximum heater temperatures were observed consistently near the center, unlike the case in conventional microgap heat sinks [32,39], where the maximum temperature occurred near the exit for single-phase flow. At low heat fluxes, there was no significant temperature difference within the heated area (~5 ℃

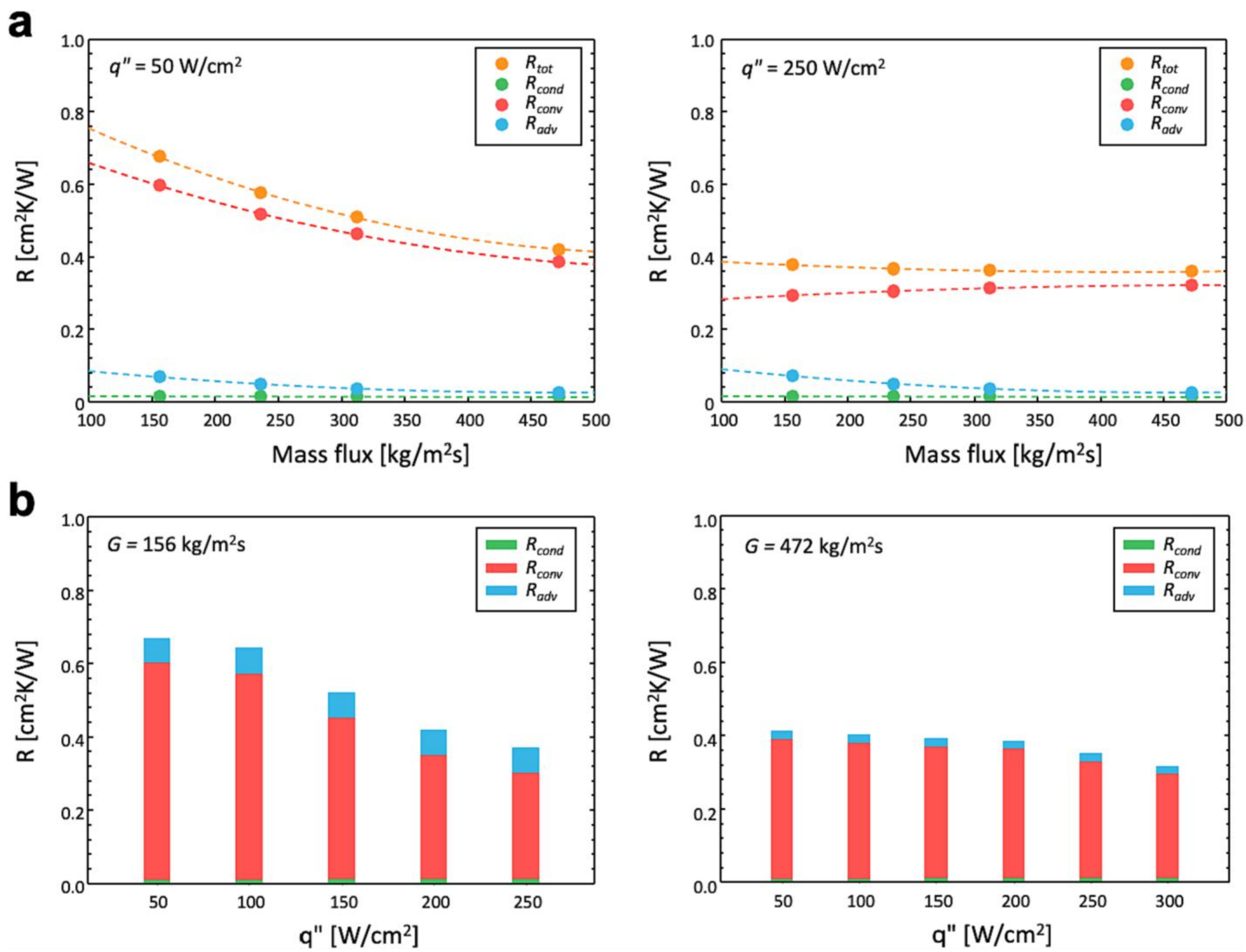

Fig. 8. Thermal resistance analysis. (a) Thermal resistance versus mass flux for heat fluxes of 50 W/cm^2 and 250 W/cm^2. (b) Breakdown of contributions of thermal resistance component under mass fluxes of 156 kg/m^2 s and 472 kg/m^2 s.

at 70 W/cm^2 under all four mass fluxes). However, the temperature difference increased considerably as the heat flux increased, and it was especially higher for higher mass fluxes. G = 156 kg/m^2 s yielded a temperature difference of 7.1 ℃ at q" = 224.2 W/cm^2, while G = 472 kg/m^2 s yielded a temperature difference of 20.3 ℃ at a similar heat flux of q" = 226.1 W/cm^2. The higher mass flux yielded a higher temperature difference owing to the non-uniform flow supply through the manifold, but this difference decreased once boiling occurred. This trend can be observed more clearly in Fig. 7(a), which illustrates ΔT_h with respect to the heat flux, where ΔT_h was obtained by subtracting the maximum temperature from the average temperature of the heated area. The maximum heater temperature was obtained from the maximum temperature points captured in the thermal images, while the average heater temperature was calculated by averaging the temperature value over the entire heater area. In the single-phase region with low heat flux, ΔT_h decreased slightly as the mass flux increased. After the ONB, ΔT_h decreased sharply. As shown in Fig. 7(a), ΔT_h was 20.8 ℃ before the ONB (q" = 234.7 W/cm^2), but it decreased to ~15 ℃ after boiling (q" = 246.6 W/cm^2) for the mass flux of 472 kg/m^2 s. A large fluctuation in ΔT_h was recorded at the mass flux of 156 kg/m^2 s with a relatively high heat flux range. The main cause of this fluctuation in ΔT_h with heat flux was the presence of trapped bubbles within the manifold. At low mass fluxes, insufficient momentum was unable to efficiently remove these bubbles, resulting in their accumulation, which caused a localized increase in the maximum temperature. (Fig. 7(b)). When the power input was around 205 W/cm^2 for higher mass fluxes, there were no bubbles trapped at the end of the manifold inlet, and the maximum heater temperature was observed in the middle of the heated area. This trend continued even under vigorous boiling, and more bubbles were nucleated at higher heat fluxes.

Fig. 8(a) shows the change in the thermal resistance component in relation to the mass flux for the heat fluxes of 50 W/cm^2 and 250 W/cm^2. When the heat flux is low at 50 W/cm^2, R_{tot} decreased significantly with increasing mass flux. Unlike R_{cond}, which remained relatively constant regardless of the mass flux, R_{adv} and R_{conv} decreased as the mass flux increased. In particular, R_{conv} decreased rapidly as the mass flux increased. However, for a heat flux of 250 W/cm^2, as the mass flux increased, R_{conv} increased marginally. Under high heat flux conditions, R_{conv} was lower when the mass flux was low because boiling occurred more frequently compared to that under a high mass flux, leading to a decrease in the wall temperature. Fig. 8(b) presents the breakdown of each thermal resistance component for the mass fluxes of 156 and 472 kg/m^2 s accompanied by an approximate increase of 50 W/cm^2 in the heat flux. At the mass flux of 156 kg/m^2 s, R_{conv} decreased remarkably after the ONB (after 107 W/cm^2), and it was 0.60 cm^2 K/W at 50 W/cm^2 and 0.29 cm^2 K/W at 250 W/cm^2. At the mass flux of 472 kg/m^2 s, R_{conv} was almost constant in the single-phase heat transfer region, and it decreased slightly after the ONB (after 234.7 W/cm^2). As a result, at the

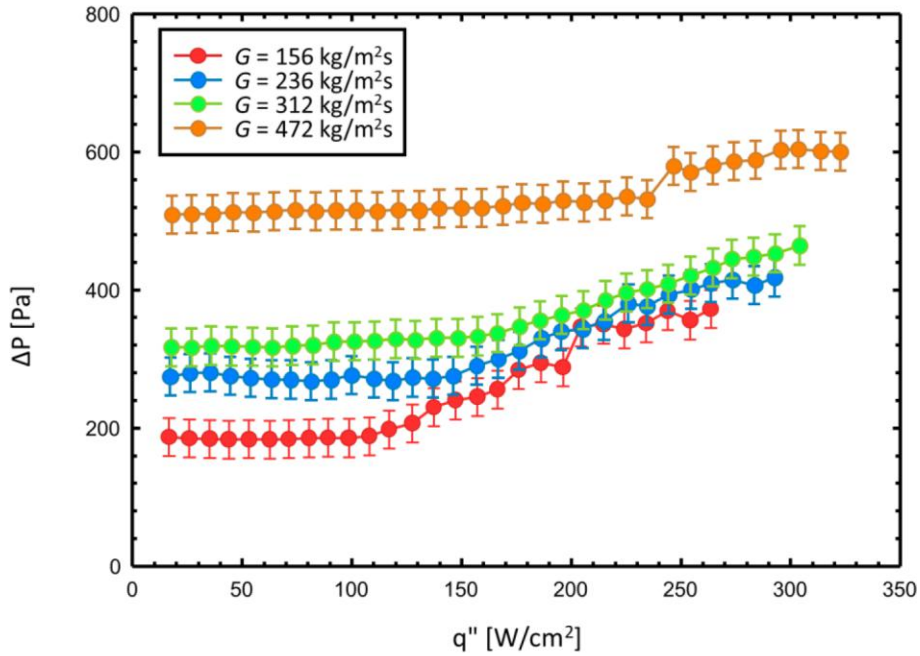

Fig. 9. Pressure drop curve with error bars as a function of heat flux. The changes in pressure drop observed within the single-phase region remained nearly uniform, but it starts increase in the high heat flux condition with boiling.

Table 2
Summary of operating conditions and geometric information from previous microgap studies.

Author	Year	Working Fluid	Inlet Temperature	Substrate	Width	Length	Gap Height	Mass Flux	Modification
Presentstudy	2023	DI Water	21 °C	Silicon	5 mm	5 mm	350 μm	156–472 kg/m^2 s	Manifold Copper inverse opal
Alam et al.	2012	DI Water	86 °C	Silicon	12.7 mm	12.7 mm	190 μm 285 μm 381 μm	420–970 kg/m^2 s	–
Dai et al.	2013	DI Water	Room temperature	Copper	5.5 mm	26 mm	340 μm	83–373.5 kg/m^2 s	Flow separation Copper woven mesh
Tamanna and Lee	2014	DI Water	91 °C	Silicon	12.7 mm	12.7 mm	200 μm 200–300 μm 200–460 μm	400–1000 kg/ m^2 s	Expanding microgap
Mathew et al.	2019	DI Water	85.5 °C	Copper	25 mm	25 mm	568 μm	100–399 kg/m^2 s	Microchannel in the upstream region
Yin et al.	2020	DI Water	65 °C	Silicon	4 mm	24 mm	250 μm	261–1861 kg/ m^2 s	Shortened micro pin–fin in the downstream region

high mass flux of 472 kg/m^2 s, R_{conv} was 0.39 cm^2 K/W at 50 W/cm^2 and 0.32 cm^2 K/W at 250 W/cm^2.

In Fig. 9, the relationship between pressure drop in the manifold microgap and the influence of heat and mass fluxes is illustrated. The changes in pressure drop observed within the single-phase region remained nearly uniform within the measurement uncertainty range. For a fixed heat flux, the pressure drop increased as the mass flux increased. After boiling occurred, the pressure drop increased owing to the incipience of nucleate bubble. Under low mass fluxes, the ONB occurred at low heat fluxes, and relatively vigorous subcooled boiling occurred, resulting in a greater increase in pressure drop than that at higher mass fluxes. Overall, despite handling a relatively high heat flux over 300 W/cm^2, the test section exhibited an impressively low pressure drop, measuring approximately 600 Pa.

3.2. Overall efficiency comparison with previous microgap studies

We conducted a comprehensive study to evaluate the established performance benchmarks of microgaps in the existing literature. Table 2 summarizes the operational parameters and geometrical data gleaned from prior microgap investigations. In Fig. 10(a,b), we illustrate the variations in thermal resistance in relation to pressure drop and pumping power. The data depicted in these figures was obtained from an experiment in which water was used as the working fluid. The R_{tot}, ΔP, and P_{pump} values corresponding to each mass flux were calculated under the maximum heat flux. As shown in this figure, the device developed herein exhibited the lowest pressure drop among all the compared devices while maintaining a decently low thermal resistance. Only Alam *et al.* [24] and Tamanna and Lee [18] reported similar ΔP values, but their R_{tot} values were higher than that reported herein. Dai *et al.* [32], Mathew *et al.* [26], and Yin *et al.* [27] reported lower R_{tot} values than that in the present study for some results. However, the pressure drops across their microgap heat sinks were one or two magnitudes higher than that observed in our study. For example, in the data of Dai *et al.* [32], where R_{tot} was similar to that reported in our study, the pressure drop was 48-fold greater than that recorded herein. Similar observations were made regarding the pumping power. In our study, R_{tot} was substantially lower than the values presented by Alam *et al.* [24], Dai *et al.*

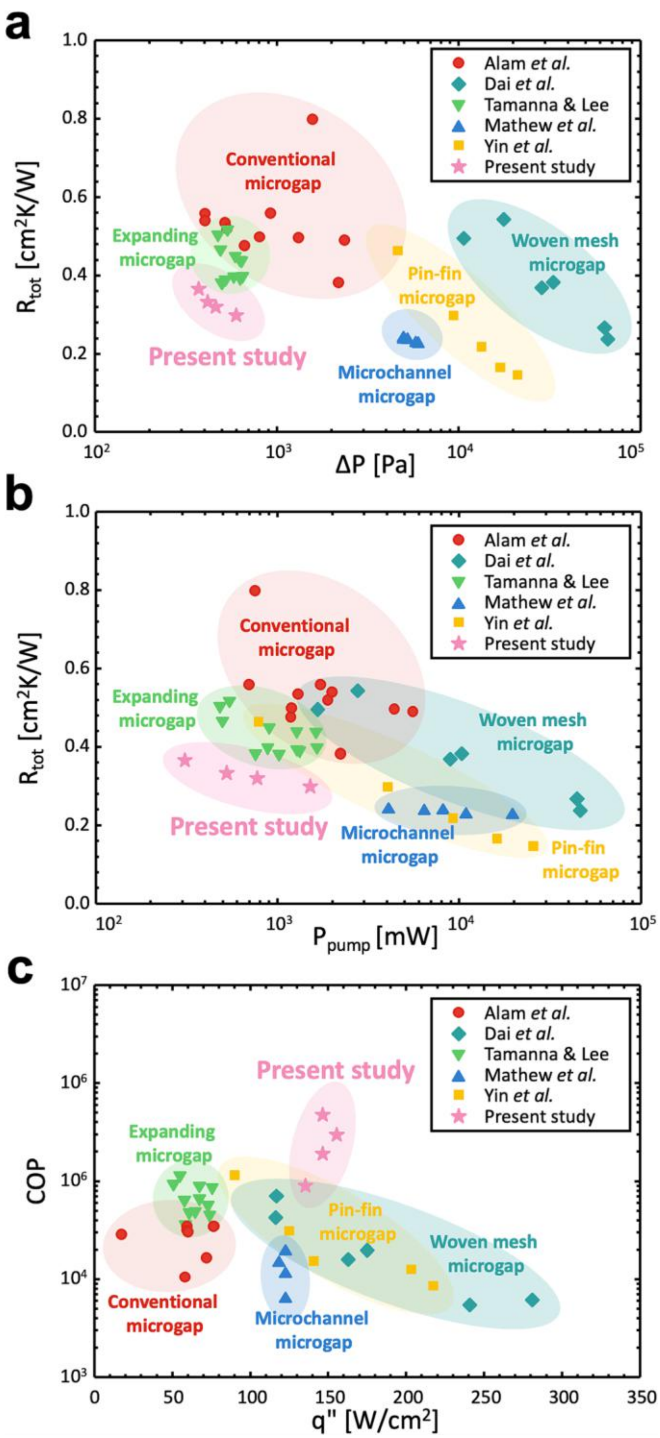

Fig. 10. Benchmark comparisons of relevant microgap studies. Thermal resistance versus (a) Pressure drop, (b) Pumping powers used in previous microgap literatures and that used in the present study, and (c) Experimentally calculated COPs of various microgap heat sinks as a function of heat flux for heater temperature rises of 25 ± 5 ℃.

[32], Tamanna and Lee [28], and Yin *et al.* [27] for similar pumping power. Fig. 10(c) illustrates the COP versus heat flux plots of other microgap studies and that of the present study. The data in this figure are identical to those in Fig. 10(a,b), except for the data pertaining to heater temperature rise below 20 ℃. As shown in this figure, the COP reported herein is considerably higher than those reported in the other microgap studies for similar heat fluxes. The data from the present study show that the mass flux of 156 kg/m^2 s had the highest COP among all the data (including other studies) with relatively high heat flux. Only Dai *et al.* [32] and Yin *et al.* [27] reported heat flux values higher than that of the present study, but they reported lower COP values than those reported herein. The manifold wall and CIO surface effectively intensified convective heat transfer and nucleate boiling. Therefore, even with a smaller pumping power than those used in other studies, our manifold microgap heat sink provided significantly superior heat transfer performance.

4. Conclusion

Herein, we developed a manifold microgap heat sink coated with CIO that effectively enhanced the heat transfer efficiency while reducing the pressure drop significantly. Subcooled flow boiling of DI water with an inlet temperature of around 21℃ and four different mass fluxes of 156–472 kg/m^2 s was tested by adjusting the heat flux in the range of 10.3–322.8 W/cm^2. The hydraulic and thermal performances of the designed manifold microgap heat sink were examined under different heat and mass fluxes. The special temperature distribution of the microgap surface was captured using an IR camera. Bubble formation during subcooled flow boiling was visualized using high-speed images. The main results of this study are as follows:

1. Maximum heat fluxes were 263.6, 292.9, 304.1, and 322.8 W/cm^2 under the mass fluxes of 156, 236, 312, and 472 kg/m^2 s, respectively. Before the ONB, the wall temperature decreased with increasing mass flux at the same heat flux, and ONB was observed at higher wall superheats with an increase in the mass flux. After the ONB was reached, nucleate boiling was the predominant heat transfer mechanism, and the slopes of the boiling curve were almost comparable for various mass fluxes.
2. In the single-phase region, temperature non-uniformity decreased slightly as the mass flux increased. After the incipience of boiling, temperature non-uniformity decreased sharply. Large fluctuation in the temperature difference between the maximum and average heating temperature occurred at low mass fluxes owing to the presence of trapped bubbles within the manifold.
3. With rising heat flux, there was a marginal reduction in pressure drop within the single-phase region. This can be attributed to the decrease in water viscosity accompanying the temperature increase. Conversely, when heat flux remained steady, an upswing in mass flux resulted in heightened pressure drop. Following the onset of boiling, pressure drop surged in tandem with increasing heat flux. Despite handling a relatively high heat flux over 300 W/cm^2, the test section exhibited an impressively low pressure drop, measuring approximately 600 Pa.
4. Compared to previous relevant studies, proposed concept exhibited superior energy efficiency with a 13-fold increase in the coefficient of performance (COP), indicating that it can be a promising cooling solution for energy-efficient thermal management in electronics devices with high heat dissipation.

CRediT authorship contribution statement

Kiwan Kim: Formal analysis, Investigation, Methodology, Writing – original draft. **Daeyoung Kong:** Conceptualization, Data curation, Formal analysis, Investigation, Methodology. **Yunseo Kim:** Data curation, Formal analysis, Software, Writing – review & editing. **Bongho Jang:** Methodology, Resources. **Jungwan Cho:** Project administration, Supervision. **Hyuk-Jun Kwon:** Project administration, Supervision. **Hyoungsoon Lee:** Funding acquisition, Project administration, Supervision, Writing – review & editing.

Declaration of competing interest

The authors declare that they have no known competing financial interests or personal relationships that could have appeared to influence the work reported in this paper.

Data availability

Data will be made available on request.

Acknowledgments

This research was supported by the Challengeable Future Defense Technology Research and Development Program through the Agency For Defense Development (ADD) funded by the Defense Acquisition Program Administration (DAPA) in 2021 (No.915028201) and by the Chung-Ang University Graduate Research Scholarship in 2022.

References

[1] A. Hassan, Y. Savaria, M. Sawan, IEEE Access 6 (2018) 78790–78802, https://doi.org/10.1109/ACCESS.2018.2885285.
[2] X. Ding, Y. Zhou, J. Cheng, Trans. Electr. Mach. Syst. 3 (2019) 54–64. https://doi.org/10.30941/CESTEMS.2019.00008.
[3] Y. Han, B.L. Lau, X. Zhang, Y.C. Leong, K.F. Choo, IEEE Trans. Compon., Packag. Manufact. Technol. 4 (2014) 1441–1450, https://doi.org/10.1109/TCPMT.2014.2335203.
[4] C.S. Sharma, M.K. Tiwari, S. Zimmermann, T. Brunschwiler, G. Schlottig, B. Michel, D. Poulikakos, Appl. Therm. Eng. 138 (2015) 414–422, https://doi.org/10.1016/j.apenergy.2014.10.068.
[5] Z. He, Y. Yan, Z. Zhang, Energy 216 (2021) 119223, https://doi.org/10.1016/j.energy.2020.119223.
[6] A.J. Robinson, IEEE Trans. Comp. Packag. Technol. 32 (2009) 347–357, https://doi.org/10.1109/TCAPT.2008.2010408.
[7] A. Datta, D. Sanyal, A. Agrawal, A.K. Das, Sādhanā 44 (2019) 234, https://doi.org/10.1007/s12046-019-1201-2.
[8] R. van Erp, R. Soleimanzadeh, L. Nela, G. Kampitsis, E. Matioli, Nature 585 (2020) 211–216, https://doi.org/10.1038/s41586-020-2666-1.
[9] W. Qu, I. Mudawar, Int. J. Heat Mass Tran. 45 (2002) 2549–2565, https://doi.org/10.1016/S0017-9310(01)00337-4.
[10] K.W. Jung, E. Cho, H. Lee, C. Kharangate, F. Zhou, M. Asheghi, E.M. Dede, K. E. Goodson, J Electron. Packag. 142 (2020) 031117, https://doi.org/10.1115/1.4047846.
[11] D. Kong, Y. Kim, M. Kang, E. Song, Y. Hong, H.S. Kim, K.J. Rah, H.G. Choi, D. Agonafer, H. Lee, Case Studies Thermal Eng. 28 (2021) 101583, https://doi.org/10.1016/j.csite.2021.101583.
[12] M.E. Johns, I. Mudawar, J. Electron. Packag. – Trans. ASME 118 (1996) 264–270, https://doi.org/10.1115/1.2792162.
[13] A.Ü. Tepe, Y. Yetişken, Ü. Uysal, K. Arslan, Int. J. Heat Mass Transf. 158 (2020) 119945, https://doi.org/10.1016/j.ijheatmasstransfer.2020.119945.
[14] T. Wei, H. Oprins, V. Cherman, E. Beyne, M. Baelmans, IEEE Trans. Compon., Packag. Manufact. Technol. 10 (2020) 577–589, https://doi.org/10.1109/TCPMT.2019.2948522.
[15] C.R. Kharangate, K. Wook Jung, S. Jung, D. Kong, J. Schaadt, M. Iyengar, C. Malone, H. Lee, M. Asheghi, K.E. Goodson, J. Electron. Packag. 140 (2018) 021001, https://doi.org/10.1115/1.4039475.
[16] D. Kong, K.W. Jung, S. Jung, D. Jung, J. Schaadt, M. Iyengar, C. Malone, C. R. Kharangate, M. Asheghi, K.E. Goodson, H. Lee, Int. J. Heat Mass Transf. 141 (2019) 145–155, https://doi.org/10.1016/j.ijheatmasstransfer.2019.05.073.
[17] D. Jung, H. Lee, D. Kong, E. Cho, K.W. Jung, C.R. Kharangate, M. Iyengar, C. Malone, M. Asheghi, K.E. Goodson, H. Lee, Int. J. Heat Mass Transf. 175 (2021) 121192, https://doi.org/10.1016/j.ijheatmasstransfer.2021.121192.
[18] A. Tamanna, P.S. Lee, Int. J. Heat Mass Transf. 82 (2015) 1–15, https://doi.org/10.1016/j.ijheatmasstransfer.2014.11.047.
[19] T. Alam, P.S. Lee, C.R. Yap, L. Jin, Int. J. Heat Mass Transf. 58 (2013) 335–347, https://doi.org/10.1016/j.ijheatmasstransfer.2012.11.020.
[20] A. Bar-Cohen, C. Holloway, J. Phys.: Conf. Ser. 745 (2016) 022002, https://doi.org/10.1088/1742-6596/745/2/022002.
[21] Y. Yang, Y. Fujita, Flow boiling heat transfer and flow pattern in rectangular channel of mini-gap, in: ASME 2nd International Conference on Microchannels and Minichannels, ASMEDC, Rochester, New York, USA, 2004, pp. 573–580, https://doi.org/10.1115/ICMM2004-2383.
[22] C.-H. Kim, M.-J. Lee, C.Y. Park, J. Mech. Sci. Technol. 32 (2018) 1449–1462, https://doi.org/10.1007/s12206-018-0249-y.
[23] J. Sheehan, A. Bar-Cohen, Spatial and temporal wall temperature fluctuations in two-phase flow in microgap coolers, in: Fluid Flow, Heat Transfer and Thermal Systems, Parts A and B, ASMEDC, Vancouver, British Columbia, Canada, 2010, pp. 1701–1708, https://doi.org/10.1115/IMECE2010-40227.
[24] T. Alam, P.S. Lee, C.R. Yap, L. Jin, Int. J. Multiphas. Flow. 42 (2012) 164–174, https://doi.org/10.1016/j.ijmultiphaseflow.2012.02.007.
[25] X. Han, A. Fedorov, Y. Joshi, J. Electron. Packag. 138 (2016) 040801, https://doi.org/10.1115/1.4034317.
[26] J. Mathew, P.-S. Lee, T. Wu, C.R. Yap, Int. J. Heat Mass Transf. 135 (2019) 1167–1191, https://doi.org/10.1016/j.ijheatmasstransfer.2019.02.033.
[27] L. Yin, P. Jiang, R. Xu, H. Hu, Int. J. Heat Mass Transf. 155 (2020) 119819, https://doi.org/10.1016/j.ijheatmasstransfer.2020.119819.
[28] A. Tamanna, P.S. Lee, Int. J. Heat Mass Transf. 89 (2015) 390–405, https://doi.org/10.1016/j.ijheatmasstransfer.2015.05.057.
[29] M. Klugmann, P. Dąbrowski, D. Mikielewicz, Appl. Therm. Eng. 181 (2020) 116034, https://doi.org/10.1016/j.applthermaleng.2020.116034.
[30] T. Alam, P.S. Lee, C.R. Yap, Int. J. Heat Mass Transf. 64 (2013) 28–41, https://doi.org/10.1016/j.ijheatmasstransfer.2013.04.009.
[31] A.K.M.M. Morshed, F. Yang, M. Yakut Ali, J.A. Khan, C. Li, Appl. Therm. Eng. 32 (2012) 68–75, https://doi.org/10.1016/j.applthermaleng.2011.08.031.
[32] X. Dai, F. Yang, R. Fang, T. Yemame, J.A. Khan, C. Li, Appl. Therm. Eng. 54 (2013) 281–288, https://doi.org/10.1016/j.applthermaleng.2013.01.030.
[33] Q.N. Pham, M.T. Barako, J. Tice, Y. Won, Sci Rep. 7 (2017) 10465, https://doi.org/10.1038/s41598-017-10791-3.
[34] N. Sapoletova, T. Makarevich, K. Napolskii, E. Mishina, A. Eliseev, A. van Etteger, T. Rasing, G. Tsirlina, Controlled growth of metallic inverse opals by electrodeposition, Phys. Chem. Chem. Phys. 12 (2010) 15414, https://doi.org/10.1039/c0cp00812e.
[35] D. Kong, M. Kang, K.Y. Kim, J. Jang, J. Cho, J.B. In, H. Lee, ACS Appl. Mater. Interfaces 12 (2020) 37784–37792, https://doi.org/10.1021/acsami.0c11402.
[36] B.N. Taylor, C.E. Kuyatt, Guidelines for evaluating and expressing the uncertainty of NIST measurement results, 1994.
[37] K.P. Drummond, D. Back, M.D. Sinanis, D.B. Janes, D. Peroulis, J.A. Weibel, S. V. Garimella, Int. J. Heat Mass Transf. 117 (2018) 319–330, https://doi.org/10.1016/j.ijheatmasstransfer.2017.10.015.
[38] T. Harirchian, S.V. Garimella, Int. J. Heat Mass Transf. 51 (2008) 3724–3735, https://doi.org/10.1016/j.ijheatmasstransfer.2008.03.013.
[39] T. Alam, P.S. Lee, C.R. Yap, L. Jin, Experimental investigation of microgap cooling technology for minimizing temperature gradient and mitigating hotspots in electronic devices, in: 2011 IEEE 13th Electronics Packaging Technology Conference, IEEE, Singapore, Singapore, 2011, pp. 530–535, https://doi.org/10.1109/EPTC.2011.6184478.